

# Spatial Non-Stationary Dual-Wideband Channel Estimation for XL-MIMO Systems

Anzheng Tang\*, Jun-Bo Wang\*, Yijin Pan\*, Tuo Wu<sup>†</sup>, Chuanwen Chang<sup>‡</sup>,  
Yijian Chen<sup>§</sup>, Hongkang Yu<sup>§</sup>, and Maged El-kashlan<sup>¶</sup>

**Abstract**—In this paper, we investigate the channel estimation problem for extremely large-scale multi-input and multi-output (XL-MIMO) systems, considering the spherical wavefront effect, spatially non-stationary (SnS) property, and dual-wideband effects. To accurately characterize the XL-MIMO channel, we first derive a novel spatial-and-frequency-domain channel model for XL-MIMO systems and carefully examine the channel characteristics in the angular-and-delay domain. Based on the obtained channel representation, we formulate XL-MIMO channel estimation as a Bayesian inference problem. To fully exploit the clustered sparsity of angular-and-delay channels and capture the inter-antenna and inter-subcarrier correlations, a Markov random field (MRF)-based hierarchical prior model is adopted. Meanwhile, to facilitate efficient channel reconstruction, we propose a sparse Bayesian learning (SBL) algorithm based on approximate message passing (AMP) with a unitary transformation. Tailored to the MRF-based hierarchical prior model, the message passing equations are reformulated using structured variational inference, belief propagation, and mean-field rules. Finally, simulation results validate the convergence and superiority of the proposed algorithm over existing methods.

**Index Terms**—XL-MIMO systems, near-field effects, spatial non-stationarity, dual-wideband effects, channel estimation, Bayesian inference.

## I. INTRODUCTION

In response to the escalating demand for data transmission, the utilization of millimeter-wave (mmWave) bands has become indispensable in alleviating spectrum congestion in conventional microwave frequencies. However, high-frequency signals face significant attenuation and susceptibility to blockages. To address these challenges, massive multi-input and multi-output (MIMO) systems with hybrid beamforming architecture have been extensively adopted to compensate for notable path loss [1]. Building upon massive MIMO, the concept of extremely large-scale MIMO (XL-MIMO) has emerged as a further evolution to meet the increasing demand for higher data rates and more efficient spatial multiplexing in mmWave wireless communication systems [2], [3]. By deploying an exceptionally large number of antennas in a compact space

with either discrete or continuous aperture configurations, XL-MIMO systems aim to significantly enhance beamforming gain and spatial degrees of freedom. Crucially, the realization of these performance gains is heavily dependent on obtaining accurate channel state information (CSI), highlighting the critical role of precise channel knowledge in maximizing the potential of XL-MIMO technologies.

However, the implementation of XL-MIMO systems introduces specific challenges to channel estimation. Due to the significant increase in the array aperture, the transmission distance between the base station (BS) and users or scatterers might be smaller than the Rayleigh distance, placing users or scatterers in the near-field region of the BS [4]–[7]. In this scenario, conventional assumptions such as planar wavefronts become less applicable, and spherical wavefront effects must be considered to accurately characterize the channels. Additionally, the extensive array aperture causes different portions of the array to observe the propagation environment from varying perspectives, giving rise to the spatial non-stationary (SnS) property [8], [9]. These novel channel characteristics, including the impact of spherical wavefronts and the SnS property, pose new challenges to channel estimation, demanding even more sophisticated approaches to manage the unique propagation dynamics in mmWave XL-MIMO systems.

Furthermore, mmWave XL-MIMO systems typically employ large system bandwidths through orthogonal frequency division multiplexing (OFDM) to exploit the rich spectrum resources in high-frequency bands, which introduces additional channel estimation challenges. On one hand, under the fifth-generation (5G) New Radio (NR) specifications [10], the maximum system bandwidth can extend up to 2 GHz, leading to a relatively small OFDM symbol duration, which may cause the propagation delay difference across the antenna array to exceed the symbol duration, giving rise to the spatial wideband effect [11], [12]. On the other hand, due to the differences in central frequencies for different subcarriers, the channels under different subcarriers experience different phase shifts, which is called the frequency-wideband effect. Considering these two effects, i.e., the *dual-wideband effects*, the correlation between antennas and between subcarriers should be carefully exploited, making the problem of channel estimation much more intractable.

### A. Related Works

Although numerous methods have been proposed to estimate channels in XL-MIMO systems, most are tailored for narrowband systems [13]–[16]. Even the sporadic works

A. Tang, J. Wang and Y. Pan are with the National Mobile Communications Research Laboratory, Southeast University, Nanjing 210096, China. (E-mail: {anzhengt, jbwang, and panyj}@seu.edu.cn)

T. Wu is with the School of Electrical and Electronic Engineering, Nanyang Technological University, 639798, Singapore (E-mail: tuo.wu@ntu.edu.sg).

Chuanwen Chang is with Nanjing Les Electronic Equipment Company Ltd., Nanjing 210014, China (E-mail: cwchang28@foxmail.com;).

Y. Chen and H. Yu are with the Wireless Product Research and Development Institute, ZTE Corporation, Shenzhen 518057, China. (E-mail: {yu.hongkang, chen.yijian}@zte.com.cn)

M. El-kashlan is with the School of Electronic Engineering and Computer Science, Queen Mary University of London, London E1 4NS, U.K. (E-mail: maged.elkashlan@qmul.ac.uk).

that consider wideband channels, such as [17], mainly address spherical wavefront effect while overlooking the dual-wideband effects and the SnS property. Specifically, [17] addresses the spherical wavefront effect by proposing a polar-domain codebook based on two-dimensional (2D) angular-distance samples. By exploiting the common polar-domain sparsity of different subcarrier channels, the wideband XL-MIMO channels are estimated using the simultaneous orthogonal matching pursuit (SOMP) method.

With the increase in bandwidth and array aperture in mmWave XL-MIMO systems, dual-wideband effects become more significant, making the common sparsity among different subcarriers less applicable. To address this issue, [12], [18] proposed gridless sparse Bayesian learning (SBL) and deep learning (DL)-based SBL algorithms, respectively, by utilizing the variations of the sparsity pattern with subcarriers in the angular domain. Additionally, super-resolution-based channel estimation algorithms have been proposed in [19]–[21] to improve estimation performance by exploiting angular-delay domain sparsity. However, these methods are tailored for far-field channels, and the proposed method cannot be extended to near-field channels intuitively. More recently, channel estimation schemes that consider both the spherical wavefront effect and dual-wideband effects have been studied in [22], [23]. Specifically, [22] proposed a bilinear pattern detection (BPD)-based approach to accurately recover wideband XL-MIMO channels, while [23] introduced a hybrid message passing algorithm based on the constrained Bethe free energy minimization framework. Despite these advancements, the SnS property has not yet been taken into consideration.

To address the SnS channel estimation problem, various methods have been proposed, including subarray-wise and scatterer-wise estimation algorithms [24], an energy detection-based algorithm [25], a group time block code (GTBC)-based algorithm [26], and Bayesian inference-based algorithms [5], [27], [28]. These works adopt a visibility region (VR)-based SnS channel model, where a VR indicator vector with each entry being 0 or 1 is introduced to characterize the SnS properties of different propagation paths. However, the assumption that the indicator variable is either 0 or 1 is idealistic and fails to capture the power variations among antennas within the VR in multipath propagation environments [9].

### B. Motivations and Contributions

Due to the randomness of the environment and user locations, spherical wavefront effect and spatial non-stationary (SnS) property exist simultaneously in wideband XL-MIMO systems. However, jointly considering the spherical wavefront effect, SnS property, and dual-wideband effects in the channel estimation problem can be an extremely challenging issue, which Unfortunately, have not been well addressed. Specifically, the channel model for SnS dual-wideband XL-MIMO channels is not well-established, and the characteristics of these channels in the angular and delay domains have yet to be thoroughly investigated. Furthermore, with the increasing number of antennas and subcarriers in XL-MIMO systems, there is an urgent need for computationally efficient channel estimation algorithms. To address these issues, this paper

investigates channel estimation for XL-MIMO systems by incorporating the spherical wavefront effect, SnS property, and dual-wideband effects. The main contributions of this paper are summarized as follows.

- Motivated by the measurement results in [9], we first derive a novel spatial-and-frequency domain XL-MIMO channel model taking spherical wavefront effect, SnS property, and dual-wideband effects into considerations. To achieve more efficient channel estimation, we carefully investigate the sparsity structure of SnS dual-wideband XL-MIMO channels in angular-and-delay domain. Specifically, the effects of spherical wavefront, SnS property, and dual-wideband phenomena on the angular and delay spread are systemically analyzed.
- Utilizing the sparsity property in angular-and-delay domain, the XL-MIMO channel estimation is formulated as a Bayesian inference problem, where a novel Markov random field (MRF) based sparse prior model is employed to fully exploit the clustered-sparsity structure of angular-delay channels, facilitating the utilization of inter-antenna and subcarrier correlations.
- To efficiently achieve Bayesian inference, we propose a sparse Bayesian learning (SBL) algorithm based on approximate message passing (AMP) with a unitary transformation. Tailored to the MRF-based hierarchical prior model, the message passing equations are reformulated using structured variational inference, belief propagation, and mean-field rules. Compared to conventional SBL algorithms, the proposed UAMP-SBL-MRF algorithm exhibits significant superiority in computational complexity, as it does not involve matrix inverse operations.

### C. Organization and Notations

The rest of the paper is organized as follows. In Section II, we present the system model as well as formulate a novel channel model of XL-MIMO systems considering the SnS property, spherical wavefront effect, and dual-wideband effects. In Section IV, we derive the channel estimation problem as a sparse signal recovery problem based on the Bayesian inference framework. In Section V, we present the proposed UAMP-SBL-MRF algorithm. Simulation results and conclusion are given in Section VI and VII, respectively.

Notations: lower-case letters, bold-face lower-case letters, and bold-face upper-case letters are used for scalars, vectors and matrices, respectively; The superscripts  $(\cdot)^T$  and  $(\cdot)^H$  stand for transpose and conjugate transpose, respectively;  $\text{diag}(x_1, x_2, \dots, x_N)$  denotes a diagonal matrix with  $\{x_1, x_2, \dots, x_N\}$  being its diagonal elements;  $\odot$  denotes the Hadamard product;  $\mathbf{I}_n$  denotes a  $n \times n$  identity matrix;  $\mathbb{C}^{m \times n}$  denotes a  $m \times n$  complex matrix. In addition, a random variable  $x \in \mathbb{C}$  drawn from the complex Gaussian distribution with mean  $x_0$  and variance  $v$  is characterized by the probability density function  $\mathcal{CN}(x; m, v) = \exp\{-|x - m|^2/v\}/\pi v$ ; a random variable  $\gamma \in \mathbb{R}$  from Gamma distribution with mean  $a/b$  and variance  $a/b^2$  is characterized by the probability density function  $\mathcal{Ga}(\gamma; a, b) = \gamma^{a-1} \exp(-\gamma b)$ ;  $m_{n_a \rightarrow n_b}(x)$  indicates a message passed from node  $n_a$  to node  $n_b$ , where the message is a function of  $x$ .

## II. SYSTEM MODEL

Consider an mmWave XL-MIMO system, where the base station (BS) utilizes the hybrid precoding architecture. The antenna array, comprising  $N_R$  antennas arranged in a uniform linear array (ULA) geometry, is connected to  $N_{RF} \ll N_R$  radio frequency (RF) chains through phase shifters to serve a single-antenna user. Denote  $\mathcal{N}_R = \{0, 1, \dots, N_R - 1\}$  as the set of all antennas at the BS side. Additionally, let  $d = \lambda_c/2$  represent the antenna spacing, where  $\lambda_c = c/f_c$ , with  $c$  and  $f_c$  indicating the speed of light and the central carrier frequency, respectively. To combat frequency-selective fading, OFDM technology is considered, where the beams implemented by phase shifters are shared by all subcarriers. Assume that  $K$  subcarriers are uniformly selected from all subcarriers to carry pilots for channel estimation, and the channels of the remaining subcarriers carrying data symbols can be obtained by interpolation. The set of all pilot subcarriers is denoted as  $\mathcal{K} = \{1, 2, \dots, K\}$ . Consider that time division duplex (TDD) based uplink and downlink transmissions are adopted. Thus, only the uplink channel needs to be estimated owing to channel reciprocity [18]. Specifically, in the uplink channel estimation phase, the user transmits the pilot signals, and the BS combines the received pilot signals using all RF chains associated with different codewords from a codebook. Denote the total number of received codeword as  $M_R$ , and consider  $M_R$  an integer multiple of  $N_{RF}$ . As a result, the BS needs  $P = M_R/N_{RF}$  time slots to traverse all received codeword given a fixed transmit symbol. Denote  $s_{k,p}$  as the pilot symbol of the  $k$ -th subcarrier in the  $p$ -th time slot. Then, the received signal at the BS of the  $k$ -th subcarrier in the  $p$ -th time slot can be expressed as

$$\mathbf{y}_{k,p} = \mathbf{W}_p \mathbf{h}_k s_{k,p} + \mathbf{n}_{k,p}, \quad (1)$$

where  $\mathbf{W}_p \in \mathbb{C}^{N_{RF} \times N_R}$  and  $\mathbf{h}_k \in \mathbb{C}^{N_R \times 1}$  denote the combining matrix in the  $p$ -th time slot and channel vector for the  $k$ -th subcarrier, respectively;  $\mathbf{n}_{k,p} \sim \mathcal{CN}(\mathbf{n}_{k,p}; 0, \beta^{-1} \mathbf{I}_{N_R})$  denotes the equivalent noise vector of the  $k$ -th subcarrier in the  $p$ -th time slot. Without loss of generality, assume the all-one pilot symbols are adopted, i.e.,  $s_{k,p} = 1$  for all  $k$  and  $p$ . Collecting all  $P$  received pilot symbols corresponding to all receive beams, the received signal in the  $k$ -th subcarrier can be written as

$$\mathbf{y}_k = \mathbf{W} \mathbf{h}_k + \tilde{\mathbf{n}}_k, \quad (2)$$

where  $\mathbf{W}$  and  $\mathbf{n}_k$  are the collective receive combining matrix and the effective noise vector with  $\mathbf{W} = [\mathbf{W}_1^T, \dots, \mathbf{W}_P^T, \dots, \mathbf{W}_P^T]^T \in \mathbb{C}^{M_R \times N_R}$  and  $\mathbf{n}_k = [\mathbf{n}_{k,1}^T, \dots, \mathbf{n}_{k,p}^T, \dots, \mathbf{n}_{k,p}^T]^T \in \mathbb{C}^{M_R \times 1}$ , respectively. Furthermore, collecting the received signals corresponding to different pilot subcarriers, the overall received signals  $\mathbf{Y} = [\mathbf{y}_1, \dots, \mathbf{y}_k, \dots, \mathbf{y}_K] \in \mathbb{C}^{M_R \times K}$  are given by

$$\mathbf{Y} = \mathbf{W} \mathbf{H} + \tilde{\mathbf{N}}, \quad (3)$$

where  $\mathbf{H} = [\mathbf{h}_1, \dots, \mathbf{h}_k, \dots, \mathbf{h}_K] \in \mathbb{C}^{N_R \times K}$  and  $\mathbf{N} = [\mathbf{n}_1, \dots, \mathbf{n}_k, \dots, \mathbf{n}_K] \in \mathbb{C}^{M_R \times K}$  indicating the channel matrix and effective noise matrix, respectively.

## III. SNS DUAL-WIDEBAND XL-MIMO CHANNEL MODEL

To jointly consider the SnS property, spherical wavefront effect, and dual-wideband effects, we derive a novel spatial-and-frequency channel model. Then, the angular-and-delay characteristics of SnS dual-wideband XL-MIMO channels are analyzed from angular spread and delay spread perspectives.

### A. Channel Modeling

Due to the large array aperture, the distance between BS and user or scatterers might be less than the Rayleigh distance determined by the array size of the BS. Consequently, the spherical wavefront effect should be considered. Additionally, in XL-MIMO systems, antenna elements at different spatial positions may observe distinct channel multipath characteristics, leading to the SnS property. Hence, the SnS property should also be incorporated into the channel modeling. For ease of illustration, we assume that there are  $L$  SnS spherical propagation paths between the transmitter array and the user. Denote  $\mathcal{L} = \{0, 1, \dots, L - 1\}$  as the set of all propagation paths. When  $l = 0$ , it refers to the line-of-sight (LoS) path, while  $l > 0$  indicates reflection or diffraction path, as illustrated in Fig. 1.

Denote  $\tau_{l,n}$  as the time delay of the  $l$ -th path to the  $n$ -th antenna. Then the baseband channel response corresponding to the  $n$ -th received antenna can be given by

$$h_n(t) = \sum_{l=1}^L \tilde{\alpha}_l s_{l,n} e^{-j2\pi f_c \tau_{l,n}} \delta(t - \tau_{l,n}), n \in \mathcal{N}_R, \quad (4)$$

where  $\tilde{\alpha}_l \in \mathbb{C}$  denotes the complex path gain.  $s_{l,n}$  is introduced to characterize the SnS property from the perspective of multipath propagation mechanisms, and it is modeled as [9]

$$s_{l,n} \begin{cases} = 0, n \notin \phi_l, \\ = 1, n \in \phi_l \text{ \& LoS blockage/Reflection,} \\ > 0, n \in \phi_l \text{ \& Diffraction,} \end{cases} \quad (5)$$

where  $\phi_l \subseteq \mathcal{N}_R$  denotes the visibility region (VR) of the  $l$ -th path with  $\rho_l \triangleq |\phi_l|/N_R$  indicating the proportion of the VR to entire array. In the following, we elucidate the physical mechanisms behind (5). In the case of LoS blockage, the LoS path is blocked partially from the perspective of antenna elements. According to measurement campaign performed in [9], a consistent power distribution among elements within  $\phi_l$ , while negligible power is detected outside this region. Concerning the reflection path, due to the large array aperture, electromagnetic signals might be reflected on those incomplete scatterers and propagate with the SnS property. In parallel with LoS blockage scenario, a constant power is evident within  $\phi_l$ , with virtually no power detected out of this region. Therefore, for LoS blockage and reflection scenarios,  $s_{l,n}$  is set as 1 and 0 for elements in and out of  $\phi_l$ , respectively. Regarding the diffraction scenario, alongside the visible and invisible phenomena, large power change among visible elements would happen [29]. In this case,  $s_{l,n}$  is set as 0 for  $n \notin \phi_l$  and non-negative real values changing with  $n$  for  $n \in \phi_l$ .

Assume the distance and direction of the  $l$ -th path to the reference antenna element as  $r_l$  and  $\vartheta_l$ , as illustrated in Fig. 1.

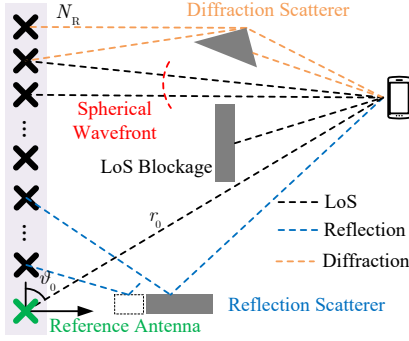


Fig. 1. Illustration of SnS spherical propagation paths.

Then,  $\tau_{l,n}$ , for any  $l \in \mathcal{L}$  and  $n \in \mathcal{N}_R$ , can be further written as

$$\tau_{l,n} = \tau_l + \frac{r_l - r_{l,n}}{c}, \quad (6)$$

where  $\tau_l = r_l/c$ ;  $r_{l,n}$  denotes the distance between the  $l$ -th scatterer ( $l = 0$  corresponds to user) and the  $n$ -th antenna element, which is defined as

$$\begin{aligned} r_{l,n} &= \sqrt{(r_l \cos \vartheta_l - nd)^2 + r_l^2 \sin^2 \vartheta_l} \\ &\stackrel{(a)}{\approx} r_l - nd \cos \vartheta_l + \frac{n^2 d^2}{2r_l} \sin^2 \vartheta_l. \end{aligned} \quad (7)$$

where (a) is obtained according to the first order Taylor expansion about  $n$ . Utilizing (7), (6) can be rewritten as

$$\tau_{l,n} = \tau_l + \frac{\psi_l}{f_c} n - \frac{\varphi_l}{f_c} n^2, \quad (8)$$

$\psi_l \triangleq d \cos \vartheta_l / \lambda_c$  and  $\varphi_l \triangleq d^2 \sin^2 \vartheta_l / 2r_l \lambda_c$ . Utilizing (6) and (7), the continuous time channel response in (4) can be further expressed as

$$h_{l,n}(t) = \sum_{l=1}^L \alpha_l s_{l,n} e^{-j2\pi(n\psi_l - n^2\varphi_l)} \delta(t - \tau_{l,n}), \quad (9)$$

where  $\alpha_l \triangleq \tilde{\alpha}_l e^{-j2\pi f_c \tau_l}$  is the equivalent complex path gain. Applying the continuous time Fourier transform to (9), the uplink spatial-frequency channel response of the user at the  $n$ -th antenna can be derived as (12), as shown in the top of next page.

Denote  $f_s$  as the total bandwidth of the OFDM system. Then, the spatial-frequency channel coefficient of the  $k$ -th subcarrier at the  $n$ -th antenna can be expressed as  $h_{l,n}(f_k)$  with  $f_k = f_c + f_s(k - 1 - (K - 1)/2)/K$  indicating the subcarrier frequency for  $k \in \mathcal{K}$ . For notation simplification, denote  $\mathbf{s}_l = [s_{l,1}, s_{l,2}, \dots, s_{l,N_R}]^T \in \mathbb{C}^{N_R \times 1}$ ,  $\mathbf{a}(\tau_l) = [1, e^{-j2\pi f_k \tau_l}, \dots, e^{-j2\pi f_k \tau_l}]^T \in \mathbb{C}^{K \times 1}$ , and  $\mathbf{b}(\psi_l, \varphi_l) = [1, e^{-j2\pi(\psi_l - \varphi_l)}, \dots, e^{-j2\pi(\psi_l(N_R-1) - \varphi_l(N_R-1)^2)}]^T \in \mathbb{C}^{N_R \times 1}$  as the indicator vector of SnS property, frequency-domain steering vector, and spatial-domain steering vector corresponding to the  $l$ -th path, respectively. In addition, the  $(n, k)$ -th entry of phase matrix  $\Theta$  is given by

$$[\Theta(\psi_l, \varphi_l)]_{n,k} = e^{-j2\pi f_k (n \frac{\psi_l}{f_c} - n^2 \frac{\varphi_l}{f_c})}. \quad (13)$$

With these notations, the overall spatial frequency channel matrix  $\mathbf{H}$  can be reformulated as

$$\mathbf{H} = \sum_{l=1}^L \alpha_l (\mathbf{s}_l \odot \mathbf{b}(\psi_l, \varphi_l) \mathbf{a}^T(\tau_l)) \odot \Theta(\psi_l, \varphi_l). \quad (14)$$

When specific effects are ignored, (14) can reduce to different channel propagation scenarios. To be specific, when  $\mathbf{s}_l = \mathbf{1}_{N_R}$  for any  $l \in \mathcal{L}$ , the spatial stationary wideband XL-MIMO channel model is obtained. When  $\mathbf{s}_l = \mathbf{1}_{N_R}$  and ignoring  $\varphi_l$ , (14) degenerates to the traditional far-field wideband MIMO channels.

**Remark 1.** Formula (14) presents a more general channel model for XL-MIMO systems, encompassing the SnS property, spherical wavefront effect, and spatial and frequency-wideband effects. In this context, the spatial-domain steering vector  $\mathbf{b}(\psi_l, \varphi_l)$  is coupled with the indicator vector of SnS property  $\mathbf{s}_l$ , the frequency-domain steering vector  $\mathbf{a}(\tau_l)$ , as well as the frequency-dependent phased matrix  $\Theta(\psi_l, \varphi_l)$ .

### B. Angular-and-Delay Representation

Due to the extensive number of antennas in XL-MIMO systems, directly estimating each entry of  $\mathbf{H}$  incurs intolerable computational complexity. Therefore, it is imperative to exploit channel sparsity in a specific transform domain. Motivated by the block sparsity observed in the angular-delay domain of wideband massive MIMO channels [11], we further investigate the sparsity characteristics of SnS dual-wideband XL-MIMO channels in the angular-delay domain in this section.

Assuming the angular domain and delay domain are uniformly sampled with  $I \geq N_R$  and  $Q \geq K$  grids, respectively, the angular-domain transformation matrix  $\mathbf{F}_A \in \mathbb{C}^{N_R \times I}$  and the delay-domain transformation matrix  $\mathbf{F}_D \in \mathbb{C}^{K \times Q}$  are essentially two oversampling DFT matrices, i.e.,  $[\mathbf{F}_A]_{n,i} = e^{-jn \frac{2\pi}{I} i} / \sqrt{N_R}$  and  $[\mathbf{F}_D]_{k,q} = e^{-jk \frac{2\pi}{Q} q} / \sqrt{K}$  with  $i \in \{0, 1, \dots, I-1\}$  and  $q \in \{0, 1, \dots, Q-1\}$ . With the aforementioned transform matrices, the channel matrix  $\mathbf{H}$  provided in (14) can be approximated as

$$\mathbf{H} \approx \mathbf{F}_A \mathbf{X} \mathbf{F}_D^H, \quad (15)$$

where the approximation error comes from the finite angular and delay resolutions of transformation matrices;  $\mathbf{X} \in \mathbb{C}^{I \times Q}$  denotes the angular-delay domain channel. Owing to the limited propagation paths,  $\mathbf{X}$  is a sparse matrix with most of its elements close to 0.

**Remark 2.** Formula (15) demonstrates that the angular-delay representation  $\mathbf{X}$  essentially is the two-dimensional inverse Fourier transform of the spatial-frequency channel  $\mathbf{H}$ . As such,  $\mathbf{X}$  comprehensively encompasses the SnS property, spherical wavefront effect, and dual-wideband effects inherent in XL-MIMO channels. Therefore, rather than directly estimating  $\mathbf{H}$ , it is more prudent to prioritize the recovery of the sparse angular-delay channel  $\mathbf{X}$  [30]. Such an approach not only promises enhanced estimation performance but also entails a reduction in computational complexity. This strategy aligns with the fundamental structural characteristics of XL-MIMO channels, facilitating the development of more efficient channel

$$h_{l,n}(f) = \int_{-\infty}^{+\infty} h_{l,n}(t) e^{-j2\pi ft} dt = \sum_{l=1}^L \alpha_l s_{l,n} e^{-j2\pi(n\psi_l - n^2\varphi_l)} e^{-j2\pi f\tau_l} e^{-j2\pi f(n\frac{\psi_l}{f_c} - n^2\frac{\varphi_l}{f_c})}. \quad (12)$$

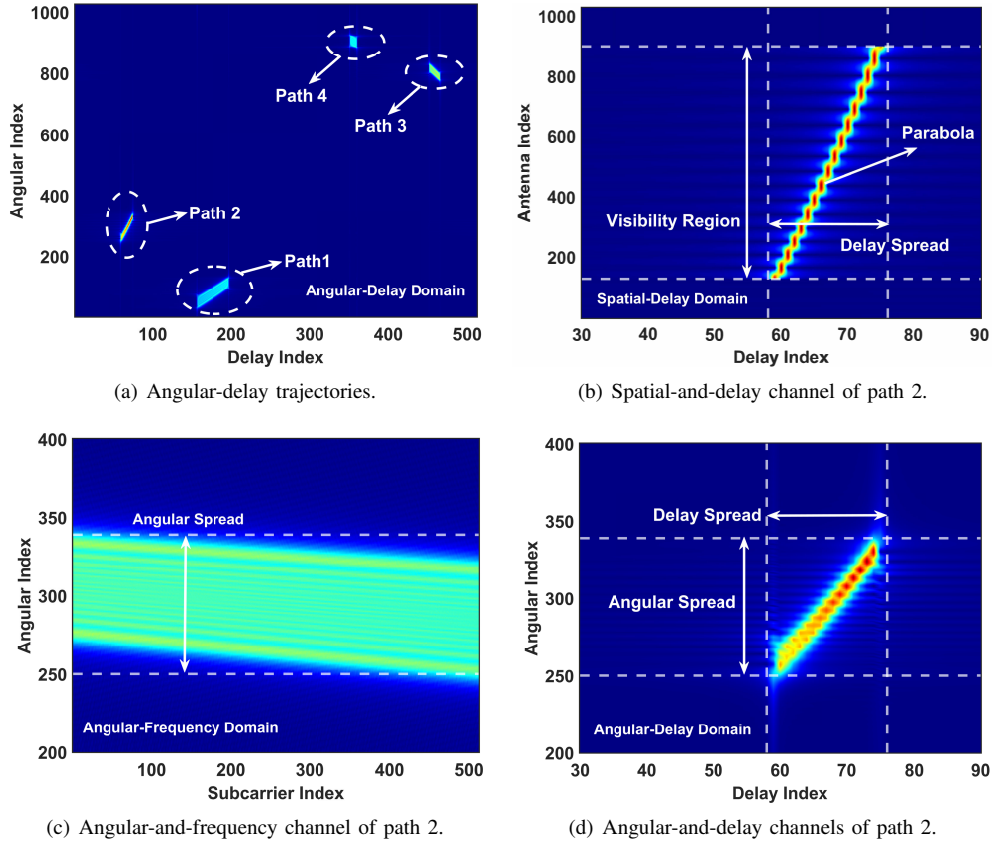


Fig. 2. Illustration of the SnS dual-wideband XL-MIMO channels in different domains.

estimation algorithms, which is of importance in practical deployment scenarios.

To intuitively investigate the effects of SnS property, spherical wavefront effect and dual-wideband effects on the angular-and-delay-domain characteristics, Fig. 2 depicts the channel representation in different domains with parameters  $N_R = I = 1024$ ,  $K = Q = 512$ ,  $f_c = 30\text{GHz}$ , and  $f_s = 3\text{GHz}$ . Take a 4-path channel as an example, where the parameters are given as follows:  $\mathbf{r} \triangleq [r_0, r_1, r_2, r_3] = [10\text{m}, 20\text{m}, 30\text{m}, 40\text{m}]$ ,  $\boldsymbol{\vartheta} \triangleq [\vartheta_0, \vartheta_1, \vartheta_2, \vartheta_3] = [\pi/6, \pi/3, 2\pi/3, 3\pi/4]$ , and  $\boldsymbol{\rho} \triangleq [\rho_0, \rho_1, \rho_2, \rho_3] = [1, 0.75, 0.5, 0.25]$ .

Fig. 2(a) illustrates the sparse representation of the SnS dual-wideband XL-MIMO channel in the angular-and-delay domain. It is evident that the angular-and-delay domain channel  $\mathbf{X}$  exhibits a cluster-sparse structure, where various propagation paths correspond to distinct clusters. This clustered-sparsity pattern of  $\mathbf{X}$  is referred to as *angular-and-delay trajectories* in this work. Comparing to traditional dual-wideband massive MIMO channels, introducing the SnS property and spherical wavefront effect in XL-MIMO channels leads to significant differences in the sparsity structure [11]. Specifically, in traditional dual-wideband massive MIMO channels,

the energy of each path diffuses to a square region, whereas in XL-MIMO channels, it forms an angular-delay trajectory. To further elaborate on the reasons behind these differences in sparsity structures, we will delve into two aspects as follows.

- **Delay spread:** Compared with traditional dual-wideband massive MIMO channels, introducing the SnS property significantly affects the range of delay spread. Specifically, the extent of visibility regions (VRs) exclusively determines the time delay range, as depicted in Fig. 2(b). The larger the VR, the more pronounced the delay spread, as illustrated in Fig. 2(a). Additionally, due to the introduction of the spherical wavefront effect, the time delay of different antennas corresponding to a specific path is proportional to the square of the antenna index  $n$  (as shown in Eq. 8). As a result, it is observed that the spatial-delay trajectory forms a parabola. Due to the linearity of the inverse discrete Fourier transform (IDFT) operation, a similar observation can be found in the angular-delay domain, as shown in Fig. 2(d).
- **Angular spread:** In traditional dual-wideband massive MIMO channels, angular spread primarily results from the frequency-dependent array response, commonly known as *beam squint* [11]. This phenomenon arises

due to variations in the array response across different subcarriers. However, in SnS dual-wideband XL-MIMO channels, angular spread is influenced by a more complex interplay of factors. Apart from beam squint effects, the spherical wavefront effects, and the SnS property contribute additional attributes to the angular spread. Specifically, the spherical wavefront effect causes the distance- and angular-dependent near-field channels, which introduces the phenomenon of angular split in angular domain, where each near-field path is associated with multiple spatial frequencies, as shown in Fig. 2(c). Additionally, the SnS property effectively reduces the effective array size. The reduction on effective array size further influences the width of angular split. Further details are available in our previous work [5].

In summary, the SnS property, spherical wavefront effect, and dual-wideband effects collectively influence the angular and delay spread of SnS dual wideband channels in angular-and-delay domains, reshaping the sparse structure of channels in the angular-delay domain from square regions to angular-delay trajectories, where different delays correspond to varying angular spreads, as shown in Fig. 2(d). However, these factors have not been fully addressed in the XL-MIMO channel estimation in current works.

#### IV. PROBLEM FORMULATION AND BAYESIAN INFERENCE

In this section, we first derive the SnS dual-wideband XL-MIMO channel estimation as a sparse signal recovery problem. Then, we introduce the three-layer sparse prior model based on the Markov random field (MRF) to capture the cluster-sparse structure of angular-and-delay-domain channel. Meanwhile, we introduce the Bayesian inference method to solve the considered channel estimation problem.

##### A. Problem Formulation

Motivated by the cluster-sparsity structure inherent in SnS dual-wideband XL-MIMO channels within the angular-delay domain, the channel estimation problem can be formulated as a sparse signal recovery problem. Utilizing the angular-delay representation in (15), the received signal model in (3) can be further written as

$$\mathbf{Y} = \mathbf{W}\mathbf{F}_A\mathbf{X}\mathbf{F}_D^H + \mathbf{N} = \mathbf{A}\mathbf{X}\mathbf{B} + \mathbf{N}, \quad (16)$$

where  $\mathbf{A} \triangleq \mathbf{W}\mathbf{F}_A \in \mathbb{C}^{M_R \times I}$  and  $\mathbf{B} \triangleq \mathbf{F}_D^H \in \mathbb{C}^{Q \times K}$ . Furthermore, stacking the columns of  $\mathbf{Y}$ ,  $\mathbf{X}$ , and  $\mathbf{N}$  yields  $\mathbf{y} = \text{vec}(\mathbf{Y}) \in \mathbb{C}^{M_R K \times 1}$ ,  $\mathbf{x} = \text{vec}(\mathbf{X}) \in \mathbb{C}^{I Q \times 1}$ , and  $\mathbf{n} = \text{vec}(\mathbf{N}) \in \mathbb{C}^{M_R K \times 1}$ . For convenience, we define  $M = M_R K$  and  $N = I Q$ . Utilizing the property of Kronecker product that  $\text{vec}(\mathbf{A}\mathbf{X}\mathbf{B}) = (\mathbf{B}^T \otimes \mathbf{A})\text{vec}(\mathbf{X})$ , (16) can be reformulated as

$$\mathbf{y} = \Phi \mathbf{x} + \mathbf{n}, \quad (17)$$

where  $\Phi = \mathbf{B}^T \otimes \mathbf{A} \in \mathbb{C}^{M \times N}$  denotes the equivalent measurement matrix. In this paper, our primary objective is to design an effective estimation algorithm to accurately reconstruct  $\mathbf{x}$  or  $\mathbf{H}$  based on  $\mathbf{y}$  and  $\Phi$ . In the literature, several sparse signal recovery algorithms have been employed to address the problem in (17), including orthogonal matching

pursuit (OMP) [31], [32] and optimization-based methods [33], [34]. Unfortunately, these methods fail to effectively exploit the cluster-sparse structure inherent in the angular-and-delay-domain channel and often require additional known parameters, such as the rank of  $\mathbf{X}$  and the number of multipaths.

##### B. Bayesian Inference

Recently, Bayesian inference has been widely adopted in channel estimation tasks [35]–[38]. However, there are two limitations in utilizing these methods for the considered SnS dual-wideband XL-MIMO channel estimation: 1) The cluster sparsity of  $\mathbf{x}$  have not been fully exploited; 2) With increasing number of antennas and subcarriers, significant computational complexity may arise due to matrix inversion operations. Specifically, the message passing based sparse Bayesian learning algorithms [35], [36] fail to adequately capture the cluster sparsity due to the utilization of a sparse prior model with the assumption that the channel coefficients are independent of each other. Additionally, the block-sparse prior based sparse Bayesian learning (SBL) algorithm involves matrix inversion operations [37], rendering its computational complexity unacceptable for XL-MIMO systems. To mitigate the computational complexity of SBL, [38] introduces an inverse-free SBL method by maximizing a relaxed evidence lower bound (ELBO). However, the relaxation in this method may lead to significant performance degradation. To address the above issues, we propose a unitary approximate message passing-based sparse Bayesian learning algorithm with an MRF-based sparse prior model, referred to as UAMP-SBL-MRF in the subsequent parts.

Since the measurement matrix  $\Phi$  may be "bad" (e.g., rank-deficient, ill-conditioned, or having a non-zero mean) [35], the divergence issues in message passing-based algorithms might be arisen. To address this, we first perform unitary transformations on the measurement matrix, i.e.,  $\Phi = \mathbf{U}\mathbf{\Lambda}\mathbf{V}^H$ . Consequently, the original signal model in (17) can be expressed as

$$\mathbf{r} = \Phi \mathbf{x} + \mathbf{w}, \quad (18)$$

where  $\mathbf{r} = \mathbf{U}^H \mathbf{y}$ ,  $\Phi = \mathbf{\Lambda}\mathbf{V}^H$ , and  $\mathbf{w} = \mathbf{U}^H \mathbf{n}$ .

To capture the cluster sparsity of the SnS dual-wideband XL-MIMO channels in the angular-and-delay domain, we adopt a three-layer sparse prior model to characterize  $\mathbf{x}$ . Specifically, the probability distribution associated with  $\mathbf{x}$  is modeled as

$$p(\mathbf{x}, \boldsymbol{\gamma}, \mathbf{s}) = p(\mathbf{x}|\boldsymbol{\gamma})p(\boldsymbol{\gamma}|\mathbf{s})p(\mathbf{s}), \quad (19)$$

where the first layer is modeled as an independent conditional Gaussian prior  $p(\mathbf{x}|\boldsymbol{\gamma}) = \prod_n p(x_n|\gamma_n)$  with  $p(x_n|\gamma_n) = \mathcal{CN}(x_n; 0, \gamma_n^{-1})$ . Note that  $\gamma_n$  is the precision parameter of channel coefficient  $x_n$ , controlling the sparsity. Specifically, when  $\gamma_n^{-1}$  approaches zero, the corresponding component  $x_n$  becomes zero. In the second layer, each  $\gamma_n$  is assigned a conditionally Bernoulli-Gamma distribution given by

$$p(\gamma_n | s_n) = \delta(1 - s_n)\Gamma(\gamma_n; a, b) + \delta(1 + s_n)\Gamma(\gamma_n; \bar{a}, \bar{b}), \quad (20)$$

where  $s_n \in \{-1, 1\}$  is a hidden state variable. When the coefficient  $x_n$  is non-zero, we have  $s_n = 1$ . Otherwise, we

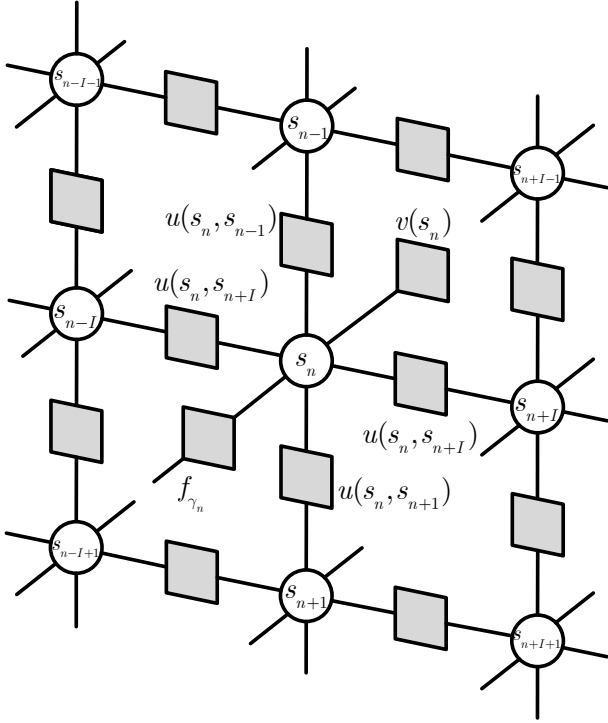


Fig. 3. Factor graph of 4-connected MRF.

have  $s_n = -1$ ;  $a$ ,  $\bar{a}$ ,  $b$ , and  $\bar{b}$  denote the shape parameters of Gamma distribution.

To capture the cluster sparsity of  $\mathbf{x}$ , the third layer is modeled as an MRF. Based on the Ising model [37], [38], the joint support  $p(\mathbf{s})$  can be modeled as

$$p(\mathbf{s}) \propto \left( \prod_n \prod_{q \in \mathcal{D}_n} u(s_n, s_q) \right)^{\frac{1}{2}} \prod_n v(s_n), \quad (21)$$

where  $\mathcal{D}_n$  is the set of neighbor nodes of  $s_n$ ,  $u(s_n, s_q) = \exp(\alpha s_n s_q)$ , and  $v(s_n) = \exp(-\eta s_n)$ ;  $\alpha$  and  $\eta$  are the parameters of the MRF. A larger  $\alpha$  implies a larger size of each cluster of non-zeros, and a larger  $\eta$  encourages a sparser  $\mathbf{x}$ . For the sparse angular-and-delay-domain channel recovery problem, we adopt a 4-connected MRF to exploit the cluster sparsity. Specifically, for each  $s_n$  in the middle of MRF, we have  $\mathcal{D}_n = \{n - I, n + I, n - 1, n + 1\}$ . The factor graph of 4-connected MRF is shown in Fig. 3, where the gray squares represent the factor nodes and the blank circles represent the variable nodes. Notably, apart from  $u(s_{n-I}, s_n)$ ,  $u(s_n, s_{n+I})$ ,  $u(s_{n-1}, s_n)$ ,  $u(s_n, s_{n+1})$ , and  $v(s_n)$ , the variable node  $s_n$  is also connected to the factor node  $f_{\gamma_n}(\gamma_n)$ .

Based on the prior distribution  $p(\mathbf{x}, \gamma, \mathbf{s})$ , the minimum mean square error (MMSE) estimator for the  $n$ -th entry of  $\mathbf{x}$ , i.e.,  $x_n$ , can be expressed as

$$\hat{x}_n = \int x_n p(x_n | \mathbf{r}) dx_n, \quad (22)$$

where  $p(x_n | \mathbf{r})$  denotes the posterior marginal probability distribution of  $x_n$ , which is defined as

$$p(x_n | \mathbf{r}) = \int p(\beta, \mathbf{z}, \mathbf{x}, \gamma, \mathbf{s} | \mathbf{r}) d\mathbf{z} d\gamma d\mathbf{s} d\mathbf{x}_{\setminus n}, \quad (23)$$

where  $\mathbf{z} \triangleq \Phi \mathbf{x}$  denotes a intermediate variable, and  $\mathbf{x}_{\setminus n}$  represents the vector  $\mathbf{x}$  without its  $n$ -th entry.  $p(\beta, \mathbf{z}, \mathbf{x}, \gamma, \mathbf{s} | \mathbf{r})$  denotes the joint posterior probability of  $\beta$ ,  $\mathbf{z}$ ,  $\mathbf{x}$ ,  $\gamma$ , and  $\mathbf{s}$ , satisfying

$$p(\beta, \mathbf{z}, \mathbf{x}, \gamma, \mathbf{s} | \mathbf{r}) = \frac{p(\beta, \mathbf{z}, \mathbf{x}, \gamma, \mathbf{s}, \mathbf{r})}{p(\mathbf{r})} \propto p(\beta, \mathbf{z}, \mathbf{x}, \gamma, \mathbf{s}, \mathbf{r}) \propto p(\mathbf{r} | \mathbf{z}, \beta) p(\mathbf{z} | \mathbf{x}) p(\mathbf{x} | \gamma) p(\gamma | \mathbf{s}) p(\mathbf{s}) p(\beta), \quad (24)$$

where  $p(\beta) \propto \beta^{-1}$  denotes the noise precise level. The conditional probability distributions  $p(\mathbf{r} | \mathbf{z}, \beta)$  and  $p(\mathbf{z} | \mathbf{x})$  are respectively given by

$$p(\mathbf{r} | \mathbf{z}, \beta) = \frac{1}{(\pi\beta^{-1})^M} \exp(-\beta \|\mathbf{y} - \mathbf{z}\|^2), \quad (25)$$

$$p(z_m | \mathbf{x}) = \delta(z_m - \phi_m^T \mathbf{x}). \quad (26)$$

The dependencies of the random variables in the factorization (24) can be shown by a factor graph as depicted in Fig. 4, where  $f_\beta(\beta) \triangleq p(\beta)$ ,  $f_{r_m}(r_m, z_m, \beta) \triangleq p(r_m | z_m, \beta)$ ,  $f_{z_m}(z_m, \mathbf{x}) \triangleq p(z_m | \mathbf{x})$ ,  $f_{x_n}(x_n, \gamma_n) \triangleq p(x_n | \gamma_n)$ , and  $f_{\gamma_n}(\gamma_n, s_n) \triangleq p(\gamma_n | s_n)$ , respectively. Given the substantial number of antennas in XL-MIMO systems, problem (22) involves high-dimensional integrals, making it impractical to compute directly. To address this issue, we propose a computationally efficient algorithm in the next section.

## V. PROPOSED UAMP-SBL-MRF ALGORITHM

Following the framework of UAMP-SBL [36] and specific to the considered SnS dual-wideband channel estimation problem, we propose a UAMP-SBL-based algorithm oriented towards MRF-based sparse prior models. The UAMP-SBL-MRF algorithm iteratively updates messages between adjacent nodes and aggregates them at nodes  $x_n$  to compute corresponding posterior distributions. This approach circumvents the computationally intensive high-dimensional integrals in (22). Specifically, the UAMP-SBL-MRF algorithm can be divided into two parts: the measurement module and the MRF-based prior module, as shown in Fig. 4. In the following sections, we introduce the details of the message passing equations in these two parts.

### A. Measurement Module

Measurement module provides the MMSE estimator of  $\mathbf{x}$  from the measured signal where messages of the noise power is updated and leveraged. Its message update steps, as outlined in lines 2-12, relies on structured variational message passing principles. It involves partitioning edges in the factor graph into strong and weak subsets. Messages on weak edges are simplified using the central limit theorem and Taylor expansion, while those on strong edges are updated through belief propagation and mean field rules. Specifically, in lines 2-5, the noiseless signals  $\mathbf{z} = \Phi \mathbf{x}$  are updated. The distribution of each element  $z_m$  is obtained as  $\mathcal{CN}(z_m; \hat{z}_m, \nu_m^z)$  using messages from the variable nodes  $x_n$  and  $\beta$ , where  $\hat{z}_m$  represents the plug-in estimate of  $z_m$  with variance  $\nu_m^z$ . As the precision of the noise is unknown, it is also updated based on the messages from factor nodes  $f_{r_m}(r_m, z_m, \beta)$ . By utilizing the belief of

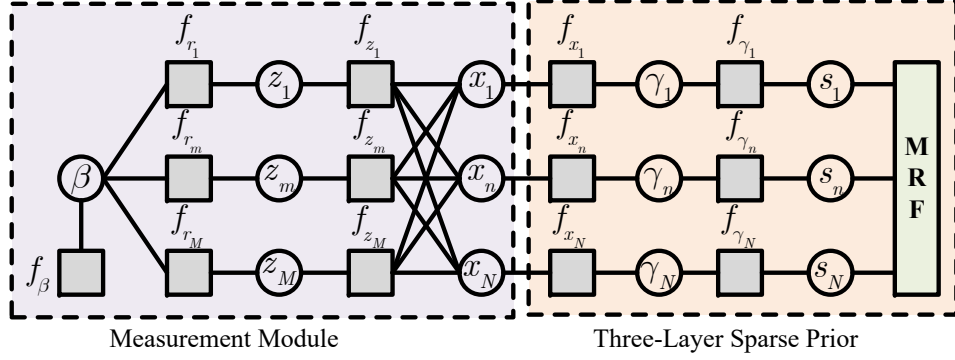


Fig. 4. Illustration of SnS spherical propagation paths between BS and user.

$b(z_m) \propto \mathcal{CN}(z_m; \hat{z}_m, \nu_m^z)$  and the mean field rule, the belief of  $\beta$  can be derived as

$$\begin{aligned} b(\beta) &\propto f_\beta(\beta) \prod_m \exp \left\{ \int b(z_m) \ln f_{r_m}(r_m, z_m, \beta) dz_m \right\} \\ &= \beta^{M-1} \exp \left\{ -\beta \sum_m (|r_m - \hat{z}_m|^2 + \nu_m^z) \right\}. \end{aligned} \quad (27)$$

From (27), we can see that  $b(\beta)$  obeys the Gamma distribution with shape parameter  $M$  and  $\sum_m (|r_m - \hat{z}_m|^2 + \nu_m^z)$ , which leads to Line 6 of the UAMP-SBL-MRF algorithm.

---

**Algorithm 1** Proposed UAMP-SBL-MRF algorithm

---

**Input:** received vector  $\mathbf{r}$ , measurement matrix  $\Phi$  and  $\mathbf{A} = \mathbf{U}\mathbf{\Lambda}\mathbf{V}^H$ ; Define  $\boldsymbol{\lambda} = \mathbf{A}\mathbf{A}^H\mathbf{1}$ .

**Initialize:**  $\tau_x^{(0)} = 1$ ,  $\hat{\mathbf{x}} = \mathbf{0}$ ,  $\hat{\gamma} = \mathbf{1}$ ,  $\hat{\beta} = 1$ ,  $\mathbf{s} = \mathbf{0}$ , and  $t = 0$ .

1: **while** the stopping criterion is not met **do**

  /\*Measurement module\*/

- 2:  $\boldsymbol{\tau}_p = \tau_x^t \boldsymbol{\lambda}$ ;
- 3:  $\mathbf{p} = \Phi \hat{\mathbf{x}}^t - \boldsymbol{\tau}_p \odot \mathbf{s}$ ;
- 4:  $\mathbf{v}_z = \boldsymbol{\tau}_p / (1 + \hat{\beta} \boldsymbol{\tau}_p)$ ;
- 5:  $\hat{\mathbf{z}} = (\hat{\beta} \boldsymbol{\tau}_p \odot \mathbf{p}) / (1 + \hat{\beta} \boldsymbol{\tau}_p)$ ;
- 6:  $\hat{\beta} = M / (\|\mathbf{r} - \hat{\mathbf{z}}\|^2 + \mathbf{1}^T \mathbf{v}_z)$ ;
- 7:  $\boldsymbol{\tau}_s = \mathbf{1} / (\boldsymbol{\tau}_p + \hat{\beta}^{-1} \mathbf{1})$ ;
- 8:  $\mathbf{s} = \boldsymbol{\tau}_s \odot (\mathbf{r} - \mathbf{p})$ ;
- 9:  $\tau_q = N(\boldsymbol{\lambda}^H \boldsymbol{\tau}_s)^{-1}$ ;
- 10:  $\mathbf{q} = \hat{\mathbf{x}}^t + \tau_q \Phi \mathbf{s}$ ;
- 11:  $\tau_x^{t+1} = (\tau_q / N) \mathbf{1}^T (\mathbf{1} / \tau_q \hat{\gamma})$ ;
- 12:  $\hat{\mathbf{x}}^{t+1} = \mathbf{q} / (1 + \tau_q \hat{\gamma})$ ;

  /\*Prior Module\*/

- 13: Update the messages  $m_{f_{\gamma_n} \rightarrow s_n}(s_n)$  according to (33);
- 14: Update the messages  $m_n^r, m_n^t, m_n^b$ , and  $m_n^s$ ;
- 15: Update the messages  $m_{s_n \rightarrow f_{\gamma_n}}(s_n)$  according to (37);
- 16: Update  $\hat{\gamma}_n$  according to (40);
- 17:  $t = t + 1$ .

18: **end while**

**Output:**  $\hat{\mathbf{x}}^{t+1}$ .

---

After updating the noiseless signal  $z_m$  and noise precise  $\beta$ , the mean and the variance of each element in the residual signal, which is obtained by removing the estimated  $\mathbf{x}$  from  $\mathbf{r}$ , are given in lines 7-8. Subsequently, lines 9-10 give the

update of the plug-in estimate  $\mathbf{q}$  of the true signal  $\mathbf{x}$ , which is modeled as

$$\mathbf{q} = \mathbf{x} + \boldsymbol{\omega}, \quad (28)$$

where  $\boldsymbol{\omega} \sim \prod_{n=1}^N \mathcal{CN}(\omega_n; 0, \tau_n^q)$  denotes the equivalent noise vector. Then, the messages  $m_{x_n \rightarrow f_{x_n}}(x_n) \propto \mathcal{CN}(x_n; q_n, \tau_n^q)$  inputs to the prior module to update the prior distribution of  $x_n$ , i.e., the messages from  $f_{x_n}$  to  $x_n$ . Once the messages  $m_{x_n \rightarrow f_{x_n}}(x_n)$  and  $m_{f_{x_n} \rightarrow x_n}(x_n)$  are obtained, the approximate posterior marginal distribution of  $x_n$  in (24) can be approximated as

$$p(x_n | \mathbf{r}) = \frac{m_{x_n \rightarrow f_{x_n}}(x_n) p_x(x_n)}{\int m_{x_n \rightarrow f_{x_n}}(x_n) p_x(x_n) dx_n}, \quad (29)$$

where  $p_x(x_n)$  denotes the extrinsic messages from the prior module, i.e.,  $p_x(x_n) = m_{f_{x_n} \rightarrow x_n}(x_n) \propto \mathcal{CN}(x_n; 0, \hat{\gamma}_n^{-1})$ . The detailed derivation of  $m_{f_{x_n} \rightarrow x_n}(x_n)$  will be given as (41) in the prior module. Consequently, the approximate posterior mean and variance of  $x_n$  can be given by

$$\hat{x}_n = \int x_n p(x_n | \mathbf{r}) dx_n = \frac{q_n}{1 + \tau_q \hat{\gamma}_n}, \quad (30)$$

$$\tau_x^n = \int |x_n - \hat{x}_n|^2 p(x_n | \mathbf{r}) dx_n = \frac{\tau_q}{1 + \tau_q \hat{\gamma}_n}. \quad (31)$$

Performing the average operations to  $\tau_x^n$  in (31) and arranging (30) in a vector form lead to lines 11 and 12.

### B. Sparse Prior Module

Sparse prior module aims to update the extrinsic messages  $m_{f_n \rightarrow x_n}(x_n)$ , which act as the prior knowledge of  $x_n$  for measurement module. Assume the belief of  $x_n$  as Gaussian distribution, satisfying  $b(x_n) = \mathcal{CN}(x_n; \hat{x}_n, \hat{v}_n^x)$ , where  $\hat{x}_n$  and  $\hat{v}_n^x$  are the posterior mean and variance of  $x_n$  given by (30) and (31). Utilizing the structured variational message passing rule, the message from  $f_{x_n}$  to  $\gamma_n$  can be give by

$$\begin{aligned} m_{f_{x_n} \rightarrow \gamma_n}(\gamma_n) &\propto \exp \left\{ \int b(x_n) \ln f_{x_n}(x_n, \gamma_n) dx_n \right\} \\ &\propto \gamma_n \exp(-\gamma_n (|\hat{x}_n|^2 + v_n^x)). \end{aligned} \quad (32)$$

According to (32) and  $f_{\gamma_n}(\gamma_n, s_n)$ , the message  $f_{\gamma_n}$  to  $s_n$  is a Bernoulli distribution given by

$$\begin{aligned} m_{f_{\gamma_n} \rightarrow s_n}(s_n) &= \int m_{f_{x_n} \rightarrow \gamma_n}(\gamma_n) f_{\gamma_n}(\gamma_n, s_n) d\gamma_n \\ &= \pi_n^{\text{out}} \delta(1 - s_n) + (1 - \pi_n^{\text{out}}) \delta(1 + s_n), \end{aligned} \quad (33)$$



$$\begin{aligned}
\pi_n^{\text{out}} &= \frac{\int \Gamma(\gamma_n; a, b) m_{f_{x_n} \rightarrow \gamma_n}(\gamma_n) d\gamma_n}{\int \Gamma(\gamma_n; a, b) m_{f_{x_n} \rightarrow \gamma_n}(\gamma_n) d\gamma_n + \int \Gamma(\gamma_n; \bar{a}, \bar{b}) m_{f_{x_n} \rightarrow \gamma_n}(\gamma_n) d\gamma_n} \\
&= \frac{\int \gamma_n^a \exp(-\gamma_n(b + |\hat{x}_n|^2 + v_n^x)) d\gamma_n}{\int \gamma_n^a \exp(-\gamma_n(b + |\hat{x}_n|^2 + v_n^x)) d\gamma_n + \int \gamma_n^{\bar{a}} \exp(-\gamma_n(\bar{b} + |\hat{x}_n|^2 + v_n^x)) d\gamma_n} \\
&\stackrel{(a)}{\propto} \frac{a(\bar{b} + |\hat{x}_n|^2 + v_n^x)}{a(\bar{b} + |\hat{x}_n|^2 + v_n^x) + \bar{a}(b + |\hat{x}_n|^2 + v_n^x)},
\end{aligned} \tag{33}$$

$$\lambda_n^1 = \frac{\pi_{n_1}^{\text{out}} e^{-\alpha + \eta} \prod_{w \in \{l, t, b\}} \lambda_{n_1}^w + (1 - \pi_{n_1}^{\text{out}}) e^{\alpha - \eta} \prod_{w \in \{l, t, b\}} (1 - \lambda_{n_1}^w)}{(e^\eta + e^{-\eta}) \left( e^{-\alpha} \pi_{n_1}^{\text{out}} \prod_{w \in \{l, t, b\}} \lambda_{n_1}^w + e^\alpha (1 - \pi_{n_1}^{\text{out}}) \prod_{w \in \{l, t, b\}} (1 - \lambda_{n_1}^w) \right)}. \tag{35}$$

where  $\pi_n^{\text{out}}$  is defined as (33). Then, we derive the message passing in MRF. For notation simplification, we define  $s_{n_l} \triangleq s_{n-I}$ ,  $s_{n_r} \triangleq s_{n+I}$ ,  $s_{n_t} \triangleq s_{n-1}$ , and  $s_{n_b} \triangleq s_{n+1}$  as the left, right, top and bottom neighbors, respectively. The input message of  $s_n$  from left, right, top and bottom neighbors, denoted as  $m_n^l$ ,  $m_n^r$ ,  $m_n^t$ , and  $m_n^b$ , are Bernoulli distributions. Take  $m_n^l$  as an example, according to the sum-product rule, we have

$$\begin{aligned}
m_n^l &= \sum_{s_{n_l} \in \{-1, 1\}} u(s_{n_l}, s_n) v(s_n^1) m_{f_{s_{n_l}} \rightarrow s_n}(s_{n_l}) \prod_{w \in \{l, t, b\}} m_{n_1}^w \\
&\propto \lambda_n^1 \delta(1 - s_n) + (1 - \lambda_n^1) \delta(s_n),
\end{aligned} \tag{34}$$

where  $\lambda_n^1$  is given by (35), as shown in the top of this page. The other three messages,  $m_n^r$ ,  $m_n^t$ , and  $m_n^b$ , can be obtained in a similar way. With the messages of neighbors and  $v(s_i)$ , the output message of  $s_n$  can be given by

$$m_{s_n \rightarrow f_{\gamma_n}}(s_n) = \pi_n^{\text{in}} \delta(1 - s_n) + (1 - \pi_n^{\text{in}}) \delta(1 + s_n), \tag{36}$$

where

$$\pi_n^{\text{in}} = \frac{e^{-\eta} \prod_{w \in \{l, r, t, b\}} \lambda_n^w}{e^{-\eta} \prod_{w \in \{l, r, t, b\}} \lambda_n^w + e^\eta \prod_{w \in \{l, r, t, b\}} (1 - \lambda_n^w)}. \tag{37}$$

Then, the message from  $f_{\gamma_n}$  to  $\gamma_n$  can be derived as

$$\begin{aligned}
m_{f_{\gamma_n} \rightarrow \gamma_n}(\gamma_n) &= \sum_{s_n \in \{-1, 1\}} f_{\gamma_n}(\gamma_n, s_n) m_{s_n \rightarrow f_{\gamma_n}}(s_n) \\
&= \pi_n^{\text{in}} \Gamma(\gamma; a, b) + (1 - \pi_n^{\text{in}}) \Gamma(\gamma; \bar{a}, \bar{b}).
\end{aligned} \tag{38}$$

With the message  $m_{f_{x_n} \rightarrow \gamma_n}(\gamma_n)$  and  $m_{f_{\gamma_n} \rightarrow \gamma_n}(\gamma_n)$ , the belief of  $\gamma_n$  can be given by

$$\begin{aligned}
b(\gamma_n) &= m_{f_{x_n} \rightarrow \gamma_n}(\gamma_n) m_{f_{\gamma_n} \rightarrow \gamma_n}(\gamma_n) \\
&= \pi_n^{\text{in}} \gamma_n^a \exp(-\gamma_n(b + |x_n|^2 + v_n^x)) \\
&\quad + (1 - \pi_n^{\text{in}}) \gamma_n^{\bar{a}} \exp(-\gamma_n(\bar{b} + |x_n|^2 + v_n^x)).
\end{aligned} \tag{39}$$

From (39), the posterior mean of  $\gamma_n$  can be given by

$$\begin{aligned}
\hat{\gamma}_n &= \int \gamma_n b(\gamma_n) d\gamma_n = \pi_n^{\text{in}} \frac{a + 1}{b + |x_n|^2 + v_n^x} \\
&\quad + (1 - \pi_n^{\text{in}}) \frac{\bar{a} + 1}{\bar{b} + |x_n|^2 + v_n^x}.
\end{aligned} \tag{40}$$

Consequently, the message from  $f_{x_n}$  to  $x_n$  can be derived as

$$\begin{aligned}
m_{f_{x_n} \rightarrow x_n}(x_n) &\propto \exp \left\{ \int \ln f_{x_n}(x_n, \gamma_n) b(\gamma_n) d\gamma_n \right\} \\
&\propto \mathcal{CN}(x_n; 0, \hat{\gamma}_n),
\end{aligned} \tag{41}$$

which plays as the input to measurement module to update the approximate posterior distribution.

**Remark 3.** Notably, the distinction between the existing UAMP-SBL algorithms [35], [36] and our work lies in the sparse prior models. Specifically, this work adopts an MRF-based three-layer sparse prior model, whereas [35], [36] employ a two-layer sparse prior model with the assumption that the channel coefficients are independent of each other. Consequently, the message passing equations, particularly in the sparse prior module, need to be reformulated.

### C. Performance and Complexity Analysis

1) *State Evolution:* The algorithm performances of the methods based on message passing can be rigorously characterized by a scalar state evolution. To elaborate, the proposed UAMP-SBL-MRF decouples the estimation of the angular-delay vector  $\mathbf{x}$  from the received signal  $\mathbf{r}$ . According to the approximate observation model in (28), the state evolution of UAMP-SBL-MRF can be given by

$$\tau^t = \frac{N}{\mathbf{1}^H (\boldsymbol{\lambda} / (\text{MMSE}(v_x^t) \boldsymbol{\lambda} + \beta^{-1} \mathbf{1}))}, \tag{42}$$

$$\text{MMSE}(v_x^t) = \frac{1}{N} \sum_{n=1}^N \mathbb{E} \{ |x_n - \mathbb{E}(x_n | \mathbf{x} + \boldsymbol{\omega})|^2 \}, \tag{43}$$

where (42) is obtained according to lines 1, 7, and 9 in Algorithm 1. As it is intractable to obtain a closed form for (43), an alternative scheme is to simulate the denoiser with the additive Gaussian noise model (28) by varying the noise variance  $\tau^t$  [36]. This allows for the creation of a mapping table with the variance of the noise as the input and the minimum mean squared error (MMSE) as the output, i.e.,  $\text{MMSE}(v_x^t) = z(\tau^t)$ , where  $z(\cdot)$  denotes an implicit mapping function between  $\text{MMSE}(v_x^t)$  and  $\tau^t$ . Therefore, the performance of UAMP-SBL-MRF can be predicted using the evolution formula (42) and the mapping function  $z(\tau^t)$ .

TABLE I. Algorithm Comparisons

| Algorithm     | Complexity          | Sparse prior                         |
|---------------|---------------------|--------------------------------------|
| SOMP [32]     | $\mathcal{O}(TMN)$  | $\times$                             |
| StdSBL [39]   | $\mathcal{O}(TM^3)$ | two-layer sparsity-promoting prior   |
| PC-SBL [40]   | $\mathcal{O}(TM^3)$ | two-layer sparsity-promoting prior   |
| UAMP-SBL [36] | $\mathcal{O}(TMN)$  | two-layer sparsity-promoting prior   |
| VSP [37]      | $\mathcal{O}(TM^3)$ | three-layer sparsity-promoting prior |
| UAMP-SBL-MRF  | $\mathcal{O}(TMN)$  | three-layer sparsity-promoting prior |

2) *Complexity Analysis*: In the following, we provide the computational complexity analysis for the proposed UAMP-SBL-MRF algorithm. The UAMP-SBL-MRF algorithm first requires pre-processing, i.e., performing an economic SVD for  $\Phi$  and unitary transformation, with a complexity of  $\mathcal{O}(M^2N)$ . It is noted that the pre-processing can be performed offline; thus, its computational complexity need not be taken into consideration. Furthermore, examining the steps of Algorithm 1, it is evident that there is no matrix inversion involved. Thus, the most computationally intensive parts only involve matrix-vector products in lines 3 and 10, i.e.,  $\mathcal{O}(MN)$  per iteration. Consequently, the total complexity of the UAMP-MRF-SBL algorithm is  $\mathcal{O}(TMN)$ , where  $T$  denotes the number of iterations. Table I summarizes the computational complexity and the required prior information of UAMP-MRF-SBL and some other popular algorithms for sparse signal recovery. Compared with standard SBL (StdSBL) [39], pattern-coupled SBL (PC-SBL) [40], and variance state propagation (VSP) [37] methods, the proposed UAMP-SBL-MRF exhibits significant superiority in computational complexity since it does not involve matrix inversion operations. Compared with the SOMP [32] and UAMP-SBL [36] methods, the UAMP-SBL-MRF adopts an MRF-based three-layer prior model in (19) to exploit the block sparsity in angular-and-delay-domain channels.

While VSP and UAMP-SBL-MRF both utilize a three-layer sparsity-promoting prior, they differ notably in the second layer. In VSP, the conditional probability distribution  $p(\gamma|s)$  in [37] follows a Bernoulli-Gaussian distribution. This model implies that when  $s_n = -1$ ,  $\gamma_n = 0$ , effectively setting  $x_n = 0$ . However, due to phenomena like energy leakage and angular splitting [4], [11], some entries in the angular-delay channels have small values that are not exactly zero. The Bernoulli-Gaussian prior might erroneously force these entries to zero. To address this issue, the UAMP-SBL-MRF algorithm adopts a novel probability model provided in (20). This model provides a more flexible characterization of the variances  $\gamma_n$ . In summary, the UAMP-SBL-MRF approach inherits the superior advantages of both the UAMP-SBL and VSP algorithms. Its performance will be thoroughly examined in the next section.

## VI. SIMULATION RESULTS

In this section, we evaluate the performance of the proposed channel estimation scheme under various system setups. The simulation parameters are shown in Table II. In particular, we consider normalized mean square error (NMSE) as performance metrics, which is defined as  $\text{NMSE} \triangleq \|\hat{\mathbf{H}} - \mathbf{H}\|_{\text{F}}^2 / \|\mathbf{H}\|_{\text{F}}^2$ , where  $\mathbf{H}$  and  $\hat{\mathbf{H}}$  are the true channel and estimated channel, respectively. In addition, the SNR is defined in received side, which is given by  $10 \log_{10} (\|\mathbf{W}\mathbf{H}\|_{\text{F}}^2 / \|\mathbf{N}\|_{\text{F}}^2)$ .

TABLE II. Simulation Parameters

| Notations                                       | Parameters                   |
|---|------------------------------|
| Number of BS antenna $N_{\text{R}}$             | 256                          |
| Number of RF chain $N_{\text{RF}}$              | 16                           |
| Carrier frequency $f_c$                         | 30GHz                        |
| Number of pilot carriers $K$                    | 64                           |
| System bandwidth $f_s$                          | 1.6GHz                       |
| Number of channel path $L$                      | 4                            |
| Angle of arrival $\vartheta_l$                  | $\mathcal{U}(-\pi/2, \pi/2)$ |
| Distance between BS and UE or scatterers $r_l$  | [10, 50]m                    |
| Proportion of visible antenna elements $\rho_l$ | (0,1]                        |

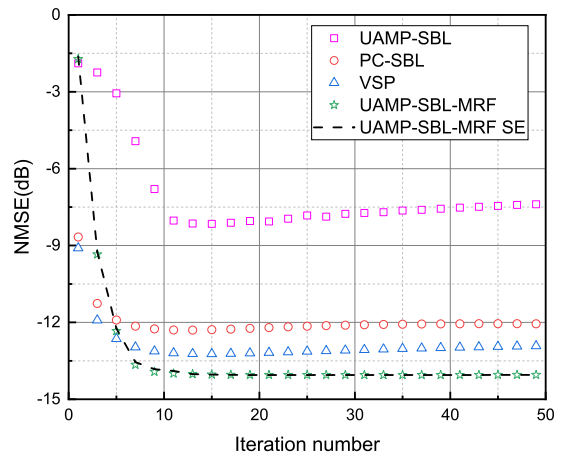


Fig. 5. Convergence behavior of different algorithms.

### A. Convergence Performance

Fig. 5 examines the convergence behavior of different estimation algorithms with  $P = 8$  and SNR = 10 dB. It is evident that the NMSE decrease with iterations for all algorithms. Notably, upon reaching the convergence criterion, the proposed UAMP-SBL-MRF algorithm demonstrates significant superiority compared to other algorithms. More extensive performance comparisons will be conducted later. Considering both performance and computational complexity, the maximum number of iterations can be safely set as 20 for subsequent simulations. Additionally, we also display the simulated performance and the evolution trajectory of UAMP-SBL-MRF. It can be observed that the simulated performance aligns well with the state evolution performance.

### B. NMSE Performance versus SNR and Pilot Symbol Number

Fig. 6 presents the NMSE performance of various algorithms versus SNR with  $P = 8$ . The results indicate that the NMSE performance of methods such as SOMP [32], StdSBL [39], and UAMP-SBL [36], which do not consider the block-sparsity structure, is significantly inferior compared to that of PC-SBL, VSP, and UAMP-SBL-MRF algorithms. Among block-sparsity prior-based algorithms, VSP [37] and the proposed UAMP-MRF-SBL outperform PC-SBL, owing to the incorporation of an MRF-based sparse prior model. Furthermore, as previously discussed, UAMP-SBL-MRF employs a more flexible variance state prior distribution, resulting in superior performance compared to VSP across the considered SNR range.

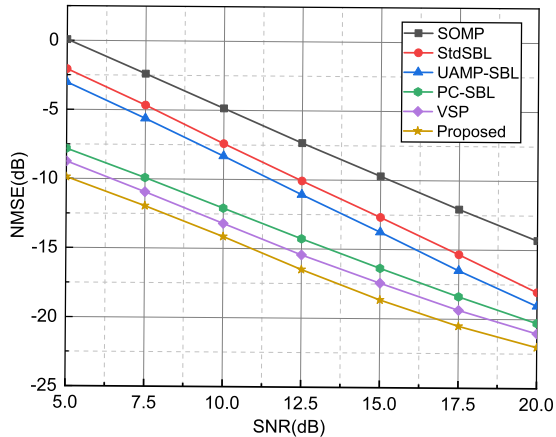


Fig. 6. NMSE performance versus SNR.

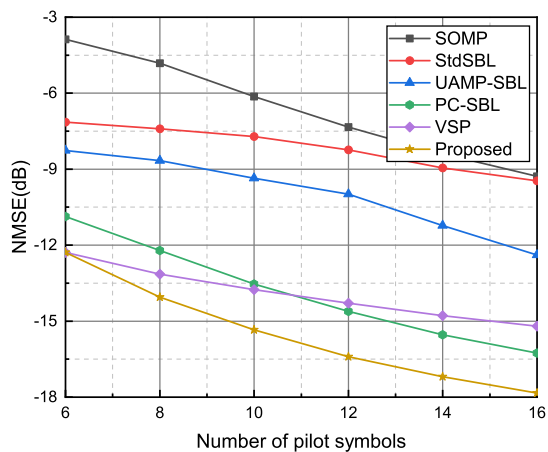


Fig. 7. NMSE performance versus pilot symbol number.

Similar performance superiority is also evident in Fig. 7, where the SNR is fixed at 10 dB. As the number of pilot symbols varies from 6 to 16, the compression ratio  $M/N$  of the measurement matrix  $\Phi$  ranges from 0.375 to 1. It is clear that in most scenarios, the proposed UAMP-SBL-MRF algorithm requires fewer pilot symbols to achieve the same performance as other algorithms. However, only when  $P = 6$  do VSP and UAMP-SBL-MRF show similar performance. Nonetheless, it is important to note that with the same number of pilot symbols, the UAMP-SBL-MRF scheme has significant advantages in computational complexity. Consequently, to balance estimation performance and computational complexity, the proposed algorithm remains a better choice even with a relatively small pilot length.

### C. NMSE Performance versus Path Number

Fig. 8 plots the NMSE performance versus the number of paths with  $P = 8$  and  $\text{SNR} = 10\text{dB}$ . Regarding the SOMP scheme, its estimation performance heavily relies on prior information about the number of propagation paths. Consequently, when the number of propagation paths varies, the SOMP algorithm designed for a specific number of propagation paths will experience severe performance degradation. In contrast, since the Bayesian inference-based schemes all utilize the sparsity-promoting prior models, their NMSE per-

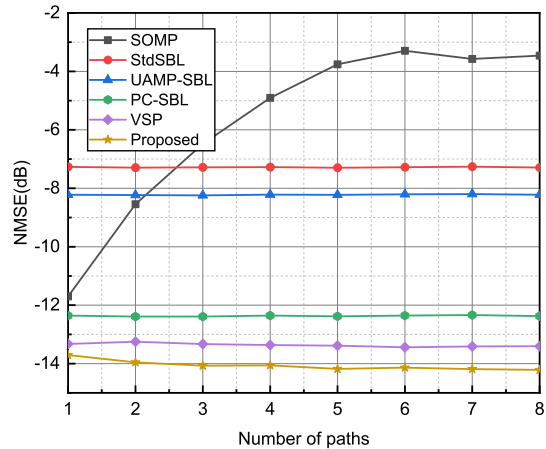


Fig. 8. NMSE performance versus path number.

formance in all considered scenarios is robust to the varying number of propagation paths. Moreover, more importantly, the performance superiority of the UAMP-SBL-MRF algorithm is generally not sensitive to the number of propagation paths.

### D. Illustration of Recovery Performance

To showcase the estimation performance of different algorithms more intuitively, Fig. 9 provides the results of a Monte Carlo simulation with  $\text{SNR} = 5\text{ dB}$  and  $P = 8$ . In this figure, the original angular-delay trajectories of a channel realization are compared with the reconstructed trajectories obtained using SOMP, StdSBL, PC-SBL, VSP, and the proposed UAMP-SBL-MRF schemes. It can be observed that the proposed UAMP-SBL-MRF algorithm provides the best visual quality with recognizable angular-delay trajectories, demonstrating its superior capability in restoring angular-delay trajectories and denoising. In contrast, the angular-delay trajectories reconstructed by SOMP exhibit poor quality, with noticeable distortion in the outline of the trajectories, particularly in the paths located in the upper left and lower right corners. While the recovery performance of StdSBL, PC-SBL, and VSP is better than that of SOMP, it remains unsatisfactory due to their limited denoising capabilities. Similar performance superiority is further demonstrated in Fig. 10, where the original spatial-delay channels and the recovered channels by different algorithms are plotted. It is evident that the proposed UAMP-SBL-MRF algorithm exhibits better performance in terms of trajectory extraction and denoising.

## VII. CONCLUSIONS

In this paper, XL-MIMO channel estimation was investigated considering near-field effects, SnS properties, and dual-wideband effects. Firstly, to accurately characterize the XL-MIMO channel, a novel SnS dual-wideband channel model was derived, and the structured sparsity in the angular-delay domain was demonstrated. Based on the proposed channel representation, the SnS dual-wideband XL-MIMO channel estimation was formulated as a Bayesian inference problem. To achieve computationally efficient Bayesian inference, a unitary approximate message passing-based sparse Bayesian learning algorithm with an MRF-based sparse prior model was

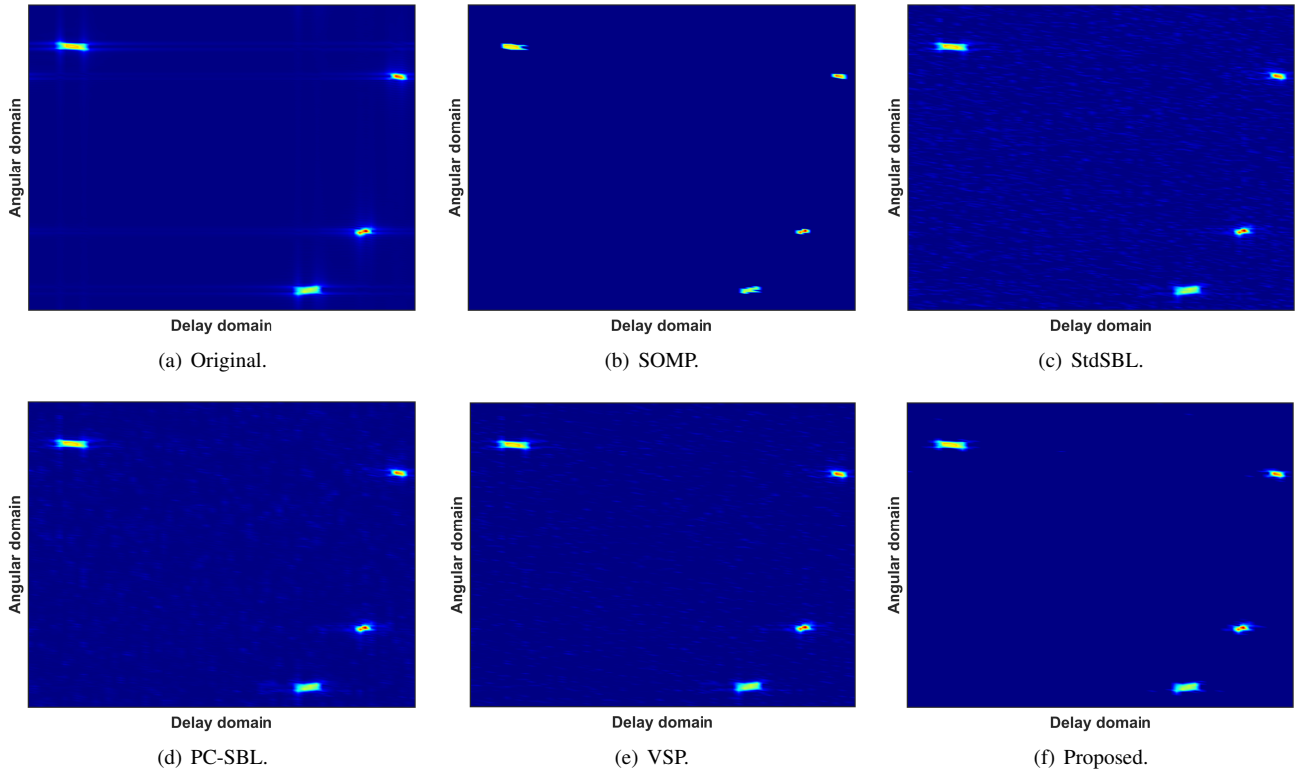


Fig. 9. Original angular-delay trajectories and the reconstructed trajectories by SOMP, StdSBL, PC-SBL, VSP, and proposed UAMP-SBL-MRF under  $\text{SNR} = 5\text{dB}$  and  $P = 8$ .

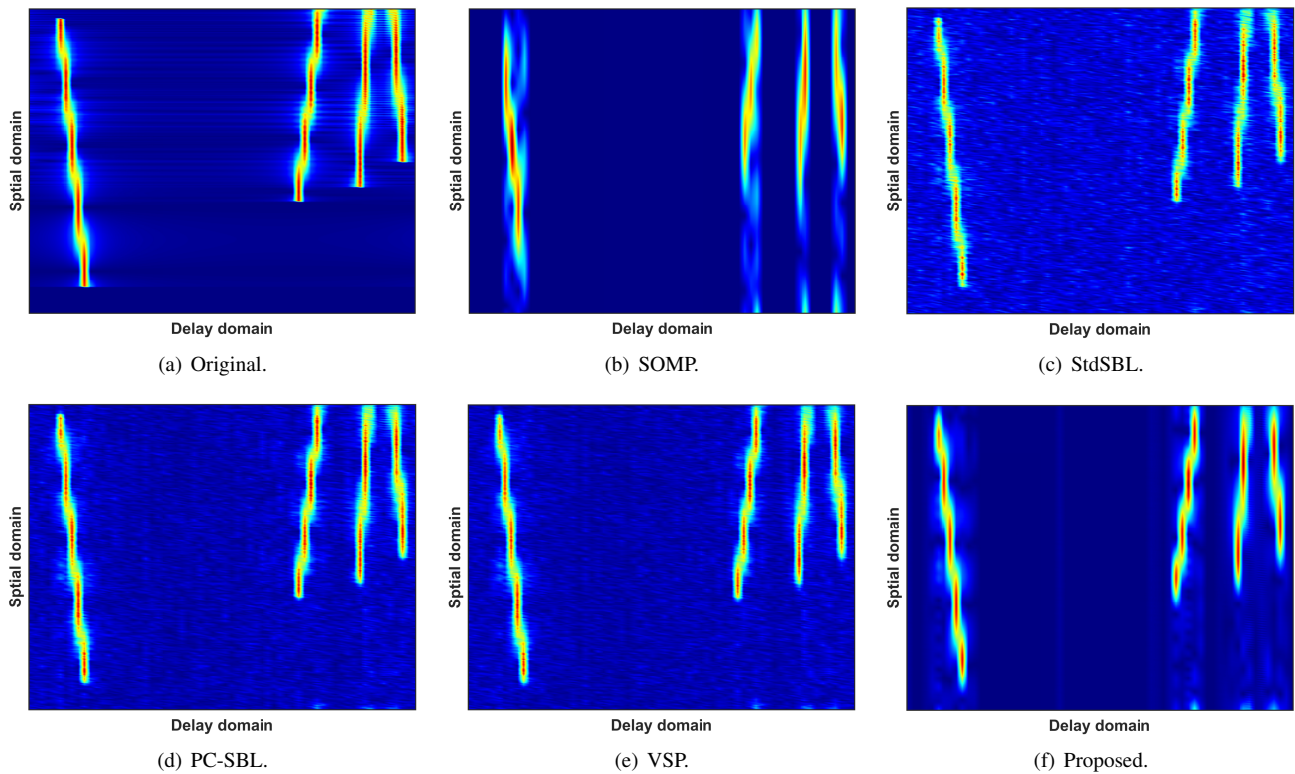


Fig. 10. Original spatial-delay channels and the reconstructed channels by SOMP, StdSBL, PC-SBL, VSP, and proposed UAMP-SBL-MRF under  $\text{SNR} = 5\text{dB}$  and  $P = 8$ .

proposed. Finally, simulation results showed that the proposed UAMP-SBL-MRF algorithm exhibits significant superiority in trajectory extraction and denoising compared to existing methods. In the future, considering the promising properties exhibited by message passing-based estimation schemes and the prevalence of graph neural networks (GNNs), the fusion of message passing and GNNs could be considered as an intriguing avenue for further research on channel estimation.

## REFERENCES

- [1] I. Ahmed, H. Khammari, A. Shahid, A. Musa, K. S. Kim, E. De Poorter, and I. Moerman, "A survey on hybrid beamforming techniques in 5G: Architecture and system model perspectives," *IEEE Commun. Surv. Tut.*, vol. 20, no. 4, pp. 3060–3097, 2018.
- [2] M. Cui, Z. Wu, Y. Lu, X. Wei, and L. Dai, "Near-field MIMO communications for 6G: Fundamentals, challenges, potentials, and future directions," *IEEE Commun. Mag.*, vol. 61, no. 1, pp. 40–46, 2023.
- [3] Z. Wang, J. Zhang, H. Du, D. Niyato, S. Cui, B. Ai, M. Debbah, K. B. Letaief, and H. V. Poor, "A tutorial on extremely large-scale MIMO for 6g: Fundamentals, signal processing, and applications," *IEEE Commun. Surv. Tut.*, pp. 1–46, 2024, early access, doi: [10.1109/COMST.2023.3349276](https://doi.org/10.1109/COMST.2023.3349276).
- [4] A. Tang, J.-B. Wang, Y. Pan, W. Zhang, Y. Chen, H. Yu, and R. C. de Lamare, "Line-of-sight extra-large MIMO systems with angular-domain processing: Channel representation and transceiver architecture," *IEEE Trans. Commun.*, vol. 72, no. 1, pp. 570–584, 2024.
- [5] A. Tang, J.-B. Wang, Y. Pan, W. Zhang, X. Zhang, Y. Chen, H. Yu, and R. C. De Lamare, "Joint visibility region and channel estimation for extremely large-scale MIMO systems," *IEEE Trans. Commun.*, pp. 1–15, 2024, early access, doi: [10.1109/TCOMM.2024.3394757](https://doi.org/10.1109/TCOMM.2024.3394757).
- [6] D. Dardari and N. Decarli, "Holographic communication using intelligent surfaces," *IEEE Commun. Mag.*, vol. 59, no. 6, pp. 35–41, 2021.
- [7] K. T. Selvan and R. Janaswamy, "Fraunhofer and fresnel distances: Unified derivation for aperture antennas," *IEEE Antennas Propag. Mag.*, vol. 59, no. 4, pp. 12–15, 2017.
- [8] E. D. Carvalho, A. Ali, A. Amiri, M. Angjelichinoski, and R. W. Heath, "Non-stationarities in extra-large-scale massive MIMO," *IEEE Wirel. Commun.*, vol. 27, no. 4, pp. 74–80, 2020.
- [9] Z. Yuan, J. Zhang, Y. Ji, G. F. Pedersen, and W. Fan, "Spatial non-stationary near-field channel modeling and validation for massive MIMO systems," *IEEE Trans. Antennas Propag.*, vol. 71, no. 1, pp. 921–933, 2023.
- [10] 3GPP, "NR; user equipment (UE) radio transmission and reception; part 2: Range 2 standalone," 2023.
- [11] B. Wang, F. Gao, S. Jin, H. Lin, and G. Y. Li, "Spatial- and frequency-wideband effects in millimeter-wave massive MIMO systems," *IEEE Trans. Signal Process.*, vol. 66, no. 13, pp. 3393–3406, 2018.
- [12] L. Xu, L. Cheng, N. Wong, Y.-C. Wu, and H. V. Poor, "Overcoming beam squint in mmWave MIMO channel estimation: A Bayesian multi-band sparsity approach," *IEEE Trans. Signal Process.*, vol. 72, pp. 1219–1234, 2024.
- [13] Z. Hu, C. Chen, Y. Jin, L. Zhou, and Q. Wei, "Hybrid-field channel estimation for extremely large-scale massive MIMO system," *IEEE Commun. Lett.*, vol. 27, no. 1, pp. 303–307, 2023.
- [14] W. Yang, M. Li, and Q. Liu, "A practical channel estimation strategy for XL-MIMO communication systems," *IEEE Commun. Lett.*, vol. 27, no. 6, pp. 1580–1583, 2023.
- [15] H. Lei, J. Zhang, H. Xiao, X. Zhang, B. Ai, and D. W. K. Ng, "Channel estimation for XL-MIMO systems with polar-domain multi-scale residual dense network," *IEEE Trans. Veh. Technol.*, vol. 73, no. 1, pp. 1479–1484, 2024.
- [16] Y. Lu and L. Dai, "Near-field channel estimation in mixed LoS/NLoS environments for extremely large-scale MIMO systems," *IEEE Trans. Commun.*, vol. 71, no. 6, pp. 3694–3707, 2023.
- [17] X. Wei and L. Dai, "Channel estimation for extremely large-scale massive MIMO: Far-field, near-field, or hybrid-field?" *IEEE Commun. Lett.*, vol. 26, no. 1, pp. 177–181, 2022.
- [18] J. Gao, C. Zhong, G. Y. Li, J. B. Soriaga, and A. Behboodi, "Deep learning-based channel estimation for wideband hybrid mmwave massive MIMO," *IEEE Trans. Commun.*, vol. 71, no. 6, pp. 3679–3693, 2023.
- [19] M. Jian, F. Gao, Z. Tian, S. Jin, and S. Ma, "Angle-domain aided UL/DL channel estimation for wideband mmwave massive MIMO systems with beam squint," *IEEE Trans. Wireless Commun.*, vol. 18, no. 7, pp. 3515–3527, 2019.
- [20] B. Wang, M. Jian, F. Gao, G. Y. Li, and H. Lin, "Beam squint and channel estimation for wideband mmWave massive MIMO-OFDM systems," *IEEE Trans. Signal Process.*, vol. 67, no. 23, pp. 5893–5908, 2019.
- [21] I.-S. Kim and J. Choi, "Spatial wideband channel estimation for mmWave massive MIMO systems with hybrid architectures and low-resolution ADCs," *IEEE Trans. Wireless Commun.*, vol. 20, no. 6, pp. 4016–4029, 2021.
- [22] M. Cui and L. Dai, "Near-field wideband channel estimation for extremely large-scale MIMO," *Science China Information Sciences*, vol. 66, no. 7, p. 172303, 2023.
- [23] H. Hou, X. He, T. Fang, X. Yi, W. Wang, and S. Jin, "Beam-delay domain channel estimation for mmWave XL-MIMO systems," *arXiv preprint arXiv:2312.05796*, 2023.
- [24] Y. Han, S. Jin, C.-K. Wen, and X. Ma, "Channel estimation for extremely large-scale massive MIMO systems," *IEEE Wireless Commun. Lett.*, vol. 9, no. 5, pp. 633–637, 2020.
- [25] Y. Han, S. Jin, C.-K. Wen, and T. Q. S. Quek, "Localization and channel reconstruction for extra large RIS-assisted massive MIMO systems," *IEEE J. Sel. Topics Signal Process.*, vol. 16, no. 5, pp. 1011–1025, 2022.
- [26] Y. Chen and L. Dai, "Non-stationary channel estimation for extremely large-scale MIMO," *IEEE Trans. Wireless Commun.*, pp. 1–15, 2023, early access, doi: [10.1109/TWC.2023.3343740](https://doi.org/10.1109/TWC.2023.3343740).
- [27] Y. Zhu, H. Guo, and V. K. N. Lau, "Bayesian channel estimation in multi-user massive MIMO with extremely large antenna array," *IEEE Trans. Signal Process.*, vol. 69, pp. 5463–5478, 2021.
- [28] H. Iimori, T. Takahashi, K. Ishibashi, G. T. F. de Abreu, D. Gonzalez G., and O. Gonsa, "Joint activity and channel estimation for extra-large MIMO systems," *IEEE Trans. Wireless Commun.*, vol. 21, no. 9, pp. 7253–7270, 2022.
- [29] R. Luebbers, "Finite conductivity uniform GTD versus knife edge diffraction in prediction of propagation path loss," *IEEE Trans. Antennas Propag.*, vol. 32, no. 1, pp. 70–76, 1984.
- [30] Y. Xu, B. Wang, E. Song, Q. Shi, and T.-H. Chang, "Low-complexity channel estimation for massive MIMO systems with decentralized baseband processing," *IEEE Transactions on Signal Processing*, vol. 71, pp. 2728–2743, 2023.
- [31] M. Cui and L. Dai, "Channel estimation for extremely large-scale MIMO: Far-field or near-field?" *IEEE Trans. Commun.*, vol. 70, no. 4, pp. 2663–2677, 2022.
- [32] J. Lee, G.-T. Gil, and Y. H. Lee, "Channel estimation via orthogonal matching pursuit for hybrid MIMO systems in millimeter wave communications," *IEEE Trans. Commun.*, vol. 64, no. 6, pp. 2370–2386, 2016.
- [33] T. Lin, X. Yu, Y. Zhu, and R. Schober, "Channel estimation for IRS-assisted millimeter-wave MIMO systems: Sparsity-inspired approaches," *IEEE Trans. Commun.*, vol. 70, no. 6, pp. 4078–4092, 2022.
- [34] J. He, H. Wymeersch, and M. Juntti, "Channel estimation for RIS-aided mmWave MIMO systems via atomic norm minimization," *IEEE Trans. Wireless Commun.*, vol. 20, no. 9, pp. 5786–5797, 2021.
- [35] L. Mo, X. Lu, J. Yuan, C. Zhang, Z. Wang, and P. Popovski, "Generalized unitary approximate message passing for double linear transformation model," *IEEE Trans. Signal Process.*, vol. 71, pp. 1524–1538, 2023.
- [36] M. Luo, Q. Guo, M. Jin, Y. C. Eldar, D. Huang, and X. Meng, "Unitary approximate message passing for sparse Bayesian learning," *IEEE Trans. Signal Process.*, vol. 69, pp. 6023–6039, 2021.
- [37] M. Zhang, X. Yuan, and Z.-Q. He, "Variance state propagation for structured sparse Bayesian learning," *IEEE Trans. Signal Process.*, vol. 68, pp. 2386–2400, 2020.
- [38] W. Xu, Y. Xiao, A. Liu, M. Lei, and M.-J. Zhao, "Joint scattering environment sensing and channel estimation based on non-stationary markov random field," *IEEE Trans. Wireless Commun.*, pp. 1–1, 2023.
- [39] M. E. Tipping, "Sparse Bayesian learning and the relevance vector machine," *Journal of machine learning research*, vol. 1, no. Jun, pp. 211–244, 2001.
- [40] J. Fang, Y. Shen, H. Li, and P. Wang, "Pattern-coupled sparse Bayesian learning for recovery of block-sparse signals," *IEEE Trans. Signal Process.*, vol. 63, no. 2, pp. 360–372, 2015.